Energy Conversion and Management 198 (2019) 111832

Contents lists available at ScienceDirect

Energy Conversion and Management

journal homepage: www.elsevier.com/locate/enconman

High frequency injection maximum power point tracking for thermoelectric generators

Romina Rodriguez[a,*], Jing Guo[b], Matthias Preindl[c], James S. Cotton[a], Ali Emadi[a]

[a] Department of Mechanical Engineering, McMaster University, Hamilton, ON, Canada
[b] BorgWarner Inc – Waterloo Technical Center, Kitchener, ON, Canada
[c] Department of Electrical Engineering, Columbia University, New York, NY, USA

ARTICLE INFO

Keywords:
DC-DC power converter
Energy harvesting
High frequency injection (HFI)
Maximum power point tracking (MPPT)
Perturb & observe (P&O)
Thermoelectric generator (TEG)

ABSTRACT

Thermoelectric generators (TEGs) can harvest thermal energy from waste heat sources to supply various power levels due to the Seebeck effect. The power generated by a TEG is dependent not only on the temperature difference across them but also on the electrical load applied. Typically, waste heat sources have variable operating conditions which means maximum power point tracking (MPPT) must be employed through the use of power converters to produce the desired operating point of the system and thus increase the system efficiency. This paper presents a new MPPT scheme which has not been previously applied to thermoelectric generators, the high frequency injection (HFI) scheme to achieve a fast and accurate tracking of the maximum power operation point for TEGs. The proposed MPPT scheme is implemented with a power converter, and the tracking scheme performance is experimentally evaluated on a commercial TEG module through three different experiments. The proposed scheme is also compared to the most commonly used MPPT scheme for TEGs, Perturb & Observe. The experimental results show that the tracking efficiency of the proposed MPPT scheme is 99.73% at steady-state compared to the ~90% tracking efficiency achieved by the Perturb & Observe scheme, as well as a 3 times faster dynamic response compared to the fastest method recorded in literature.

1. Introduction

Harvesting energy from waste heat is a method by which the overall system efficiency may be increased [1]. In the past decades, thermoelectric generators (TEGs) have gained interest as a viable technology for recovering energy that is lost to the environment in applications that range from medical [2–4] to automotive [5–9]. Thermoelectric generators are solid state devices that convert thermal energy directly into electrical energy. This phenomenon known as the Seebeck effect is observed when a voltage is generated across the junction of two conductors due to a temperature difference. The direct energy conversion is a major advantage of TEGs and other advantages include their small size, low system complexity, quiet operation and little to no maintenance [10].

The power produced by a TEG is not only dependent on the thermal operating conditions but also on the electrical load applied. Therefore, a power converter is usually interfaced with the TEGs that are connected either in series or parallel, depending on the desired voltage output of the system. To ensure that the maximum power is produced by the TEG during operation, a Maximum Power Point Tracking (MPPT) scheme is programmed to control the power converter. In waste heat recovery applications such as automotive, geothermal, industrial plants, etc., the waste heat sources are dynamic in operation, i.e. the exhaust fluids have variable temperature and mass flow rates which determine the amount of heat energy available for harvesting. Unlike other waste heat recovery technologies such as Rankine cycles (i.e. turbo-lag) [11], TEGs can operate robustly in these dynamic environments to recover energy. Consequently, MPPT algorithms need to be employed that can quickly adapt to these variable operating conditions.

The most commonly used MPPT scheme for TEGs in the literature is the Perturb & Observe (P&O) scheme which works by altering the TEG operation setpoint, observing if the output power increased or decreased and making a decision based on this information [12–15]. The main disadvantage with this method is that the maximum power point (MPP) is not reached, but instead the power output of the TEG oscillates around the MPP. The Incremental Conductance (IncCond) method considers the derivative of the power (derivative is zero at MPP) and changes the setpoint based on this feedback [16–18]. In comparison to P&O, IncCond offers a more robust quantifier on the location of the operation point. Similarly to P&O, IncCond requires a sufficiently large

* Corresponding author.
E-mail address: romina@mcmaster.ca (R. Rodriguez).

https://doi.org/10.1016/j.enconman.2019.111832
Received 9 March 2019; Received in revised form 12 July 2019; Accepted 13 July 2019
Available online 19 July 2019

Nomenclature

ΔT	temperature difference, K
A	cross-sectional area, m^2
B	amplitude
D	duty cycle
f	frequency, Hz
I	current, A
K	thermal conductance, W/K
k	thermal conductivity, W/m-K
L	length, m
P	electrical power, W
Q	heat flux, W
R	electrical resistance, Ω
T	temperature, K
V	voltage, V

Greek Symbols

α	seebeck coefficient, V/K
η	efficiency, %
ω	angular frequency, rad/s

Abbreviations

HFI	High Frequency Injection
MP	Maximum Power
MPPT	Maximum Power Point Tracking
P&O	Perturb & Observe
TEG	Thermoelectric Generator

Subscripts

C	cold side
H	hot side
int	internal
l	load
max	maximum
o	out
oc	open circuit
sw	switching

step and keeps moving around the MPP. The fractional open-circuit voltage scheme is another commonly used MPPT method in the literature. It is implemented by setting the current to 0A, measuring the open-circuit voltage of the TEG, and then setting the electrical load to half this value [19–21]. One drawback with this scheme is that the TEG needs to be disconnected from the load to measure the open circuit voltage and hence the dynamics, i.e. the operating condition of the TEG is affected.

Although other schemes are presented in the literature, the majority of the MPPT algorithms' performance is evaluated at steady-state which is not indicative of what occurs during the operation of TEGs in waste heat recovery applications. The location and mounting of the thermocouples in the MPPT method proposed by [22] adds complexity to the TEG harvesting system and introduce possible errors when finding the accurate MPP of a larger TEG system (more than one TEG module), since it depends on accurate measurements of the temperature differences. Although, [23] proposed a simpler method to find the MPP of a TEG, a setback is that the TEG system needs to be characterized prior to implementation since a pre-programed setpoint of MPPs is used by the algorithm. As the operating conditions change rapidly in waste heat recovery application such as those in the exhaust system of a vehicle [24], calibrating the system for every possible setpoint would be cumbersome.

In this paper, a new MPPT scheme is proposed, the High Frequency Injection (HFI) scheme, where a high frequency signal is injected into the system and the perturbation observed is used as feedback to control the operating condition of the TEG and arrive at the MPP, without inducing oscillations to the system. The HFI scheme requires only measurement of the TEG power, hence no additional sensors are needed such as thermocouples and the MPPT can quickly adapt to changes in the system without prior characterization. The proposed scheme is experimentally implemented and the performance is evaluated through three different experiments, including transient operation. The scheme is also experimentally compared to the most commonly used MPPT scheme, P&O.

The paper is organized as follows: Section 2 explains the physics of TEGs as well as how they were experimentally characterized. Section 3 explains the theory behind the HFI MPPT scheme and goes over the P&O scheme. Next, the experimental validation procedure is explained and the experimental results are discussed in Section 4 and 5.

2. TEG energy harvesting

The following sections describe the working principle of TEGs and demonstrate the electro-thermal characterization of a TEG module to experimentally evaluate the performance of MPPT schemes.

2.1. Working principle

Thermoelectric generators operate due to the Seebeck effect. This effect was observed when two dissimilar conductors were connected and an electromotive force (emf) was generated due to the junctions being maintained at different temperatures [25]. The Seebeck coefficient, α, is defined by the emf or open circuit voltage, V_{oc}, generated and the temperature difference, ΔT, across the thermoelectric junctions

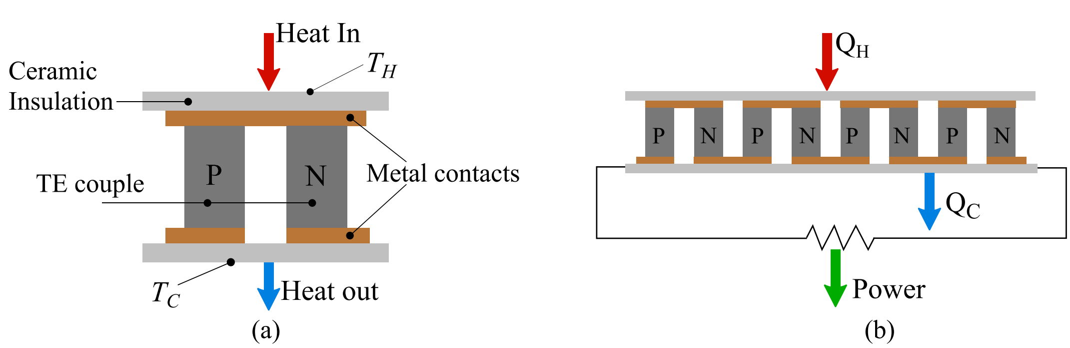

Fig. 1. (a) TE p-n couple schematic (b) Many p-n couples form a TEG module.

$$\alpha = \frac{V_{oc}}{\Delta T}. \tag{1}$$

Semiconductors generate a higher V_{oc} compared to metals, hence they are used to manufacture TEGs. A positive-doped (p-type) semiconductor is connected via a metal contactor to a negative-doped (n-type) semiconductor to create a thermoelectric (TE) junction, considered a p-n couple as shown in Fig. 1(a). When a temperature difference is applied across the TE junction, V_{oc} is generated and if an electrical load is connected, current is allowed to flow, thus generating power. At steady-state, a TEG may be modeled as a voltage source in series with an electrical internal resistance, R_{int}, as presented in Fig. 2(b). Hence, V_{oc} can be increased by joining many p-n couples in series. Thus, A TEG module consists of many p-n couples connected electrically in series and thermally in parallel as seen in Fig. 1(b).

A temperature difference is created by allowing heat to flow across the TEG module (heat source and heat sink required), therefore electrical insulation from the heat source is necessary (usually a ceramic). As heat, Q_H, flows through the TEG, the thermal conductance of the TEG, K_{TEG}, will cause a temperature difference across the TEG: T_H and T_C, the hot side and cold side, respectively. When electrical current flows through the TEG module, heat will be transferred from T_H to T_C due to the Peltier effect [25]. In general, this will cause the temperature difference to decrease which is seen as a negative effect. Finally, there are also Joule losses that are generated when current flows through the TEG.

Taking into account all these thermoelectric effects, Q_H and the heat exiting the TEG, Q_C is defined as [26]

$$Q_H = \alpha T_H I + K_{TEG}(T_H - T_C) - \frac{1}{2}I^2 R_{int} \tag{2a}$$

$$Q_C = \alpha T_C I + K_{TEG}(T_H - T_C) + \frac{1}{2}I^2 R_{int} \tag{2b}$$

where I is the current flowing through the TEG. An electrical diagram of the heat flows in the TEG and its equivalent circuit are shown in Fig. 2(a) and (b), respectively. The power generated by the TEG is then the difference between Q_H and Q_C and defined as

$$P = Q_H - Q_C \tag{3a}$$

$$= \alpha \Delta T I - I^2 R_{int}. \tag{3b}$$

Therefore, the power produced is not only dependent on the temperature difference across the TEG, but also on the current, I. The power output can be predicted with (3b), as a function of current, if α and R_{int} are known for any temperature difference.

Consider the electrical circuit of a TEG as shown in Fig. 2(b). The power produced from the TEG may also be described as

$$P = I^2 R_l \tag{4}$$

where R_l is the electrical load resistance connected to the TEG terminals. The TEG current, I, is therefore equal to

$$I = \frac{V_{oc}}{R_{int} + R_l} \tag{5}$$

and (4) can be rewritten as

$$P = \frac{V_{oc}^2}{(R_{int} + R_l)^2} R_l. \tag{6}$$

The maximum power may now be found by taking the derivative with respect to R_l

$$\frac{dP}{dR_l} = \frac{V_{oc}^2 (R_{int} - R_l)}{(R_{int} + R_l)^3} = 0. \tag{7}$$

Thus, $R_l = R_{int}$ when the TEG power is maximized and results in

$$V_{TEG} = \frac{1}{2} V_{oc}. \tag{8}$$

At maximum power, the load resistance will equal the internal resistance of the TEG, thus (6) becomes

$$P_{max} = \frac{V_{oc}^2}{(R_{int} + R_{int})^2} R_{int} = \frac{V_{oc}^2}{4R_{int}} = \frac{\alpha^2 \Delta T^2}{4R_{int}}. \tag{9}$$

The theoretical maximum power for a TEG module can now be calculated with (9) if α, R_{int} and the temperature difference across the TEG are known.

2.2. Experimental characterization setup

As explained in the previous section, a temperature difference must be imposed across the TEG and an electrical load connected to observe the power generated. The experimental test rig designed for characterization of a TEG module is seen in Fig. 3. A TEG module is compressed between two copper blocks with equal cross-sectional area. The hot block has heaters that are controlled to maintain the TEG hot side at a specified temperature. Fins were machined into the cold block and are cooled by a chiller. A force is applied to a bolt that is screwed into the cold block to maintain a fixed pressure on the TEG module. A load cell is used to measure the pressure applied to the TEG module. All the tests were completed at 530 kPa which is recommended by the TEG module datasheet.

The TEG module and copper blocks, which sandwich the module, are placed in a vacuum chamber to ensure there are no convective heat losses from the blocks to the environment. Since the hot block experiences high temperatures, a radiation shield is placed around the block to reduce thermal losses in vacuum. Thermocouples (TCs) are placed along the axial direction (y-axis in Fig. 3) of both copper blocks to record the temperature gradient. A TC is not placed between the blocks and the TEG module to directly measure T_H and T_C as this creates a hot spot and incorrect temperature measurement results. At steady-state, a temperature distribution exists only in the axial direction and T_H is derived from

$$T_H = T - \frac{L}{kA} Q \tag{10}$$

where T is the temperature reading of the closest TC to the TEG module, L is the distance between the TC and the TEG, k is the thermal conductivity of the copper block, and A is the cross-sectional area of the block which is equal to that of the TEG module. Q is the heat flux through the block which is calculated from the other TC readings at

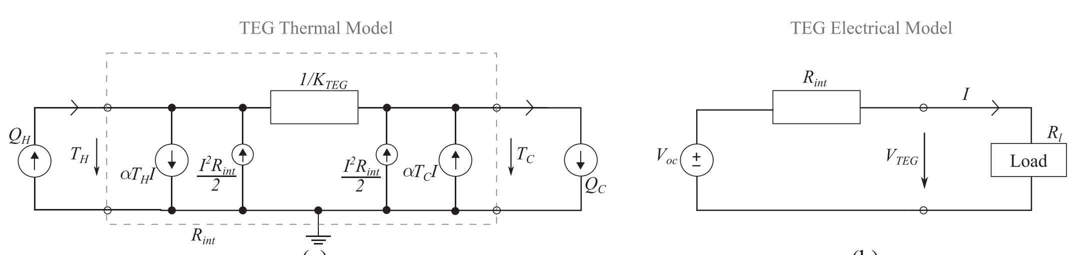

Fig. 2. (a) Equivalent electro-thermal model of TEG (b) Electrical TEG model.

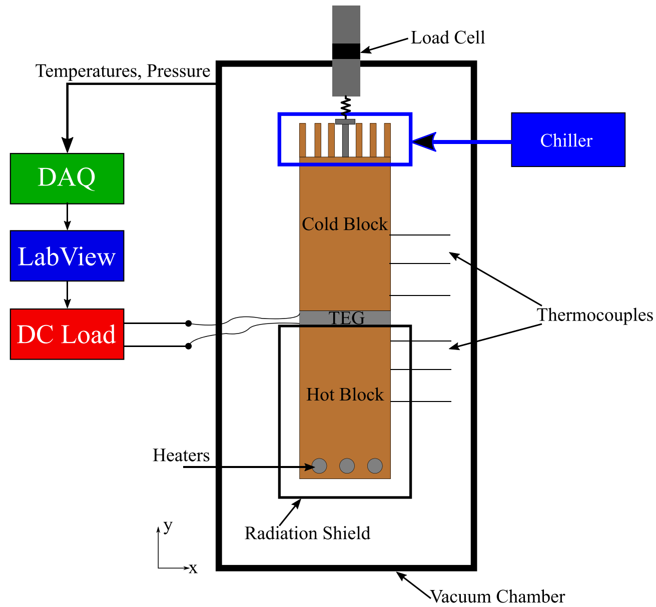

Fig. 3. Schematic of experimental setup for electro-thermal characterization (not drawn-to-scale).

steady-state. The same calculation is done to calculate the TEG cold side, T_C. When there is no current flowing through the TEG, Q_H should be equal to Q_C or similarly the heat flux through the hot copper block should be equal to the heat flux through the cold copper block. Experiments performed in this test rig showed that this is true within 2% error.

A DC load is connected to the TEG module to vary the current for the characterization. A DAQ interfaced with LabView is used to control the current imposed on the TEG, as well as the temperature difference across the TEG. The experimental characterization was performed as follows: (1) Set current, (2) PID control of heaters to fix T_H, (3) chiller setpoint is changed to achieve desired T_C, (4) wait until steady-state is achieved and record data. The results of the characterization for various temperature differences is presented in the next section.

2.3. Electro-thermal characterization

A TEG module, TEG1-12610-5.1 from TECTEG MFR was experimentally characterized for various T_H, while maintaining T_C at 35 °C. The characterization results are shown in Fig. 4. As can be observed from the graph, there exists one maximum power point (MPP) per curve and it occurs at $V_{oc}/2$. The parameters, V_{oc}, R_{int} and α are tabulated in Table 1.

Taking the parameters from Table 1, (3b) was used to generate the power profiles in Fig. 5. The maximum error between the experimental data in Fig. 4 and the model in Fig. 5 is 1.7%, but the maximum error only considering the MPP is 0.2%. Hence the parameters from Table 1 can be used to predict the maximum power as a function of temperature difference.

3. Maximum power point tracking

Two MPPT schemes were implemented to evaluate the tracking performance on the characterized TEG module. The first scheme is the commonly used Perturb & Observe scheme and the second scheme is the proposed High Frequency Injection scheme that has not been previously experimentally demonstrated. The TEG module can be electrically modeled as shown in Fig. 2(b). The power output is maximized when the load resistance is equal to the TEG internal resistance as presented by (4)–(8). The MPPT configuration for both schemes is presented in Fig. 6, where a DC/DC converter is programmed to be interfaced between the TEG module and DC load, to control the TEG power output.

3.1. Perturb & observe

The Perturb & Observe (P&O) scheme works by observing how the power output of the TEG shifts once a perturbation or setpoint change is made to the operating conditions. The sampling period, T_s, must be much larger than the electro-thermal time constants to ensure electro-thermal dynamics do not distort the power measurement. A flowchart explaining how the algorithm works is in Fig. 7.

Initially, the current reference for the converter is set to some initial value, I_{ref}, then every T_s the power is measured (the TEG power as shown in Fig. 6) and the current reference is either increased or decreased by ΔI according to either an increase or decrease in power. For the experimental validation, ΔI was chosen as 0.08A and T_s was 10 ms. Although there exists adaptive P&O schemes such that ΔI varies as the MPP is approached [27], in this work a constant ΔI was chosen for simplicity and to have a baseline reference scheme for comparison.

3.2. Proposed MPPT

Simulations for the proposed MPPT scheme were presented in IECON'15 [28]. The following paragraphs describe the mathematical formulation behind the method. The High Frequency Injection (HFI) MPPT method adds a high frequency sinusoidal signal to the operating condition of the TEG which results in a perturbation that can be controlled directly, thus choosing the operation point of the TEG. A schematic of the operation for the HFI scheme is shown in Fig. 8.

Consider, a boost converter used in the MPPT configuration of Fig. 6. The TEG output voltage, V_{TEG}, can be described as function of the DC load voltage, V_o, as

$$V_{TEG} = V_o(1 - D) \tag{11}$$

where D is the duty cycle of the switch in the power converter [29]. The output power of the TEG is then

$$P = IV_{TEG} \tag{12}$$

and I can be written as

$$I = \frac{V_{oc} - V_{TEG}}{R_{int}}. \tag{13}$$

Substituting (11) and (13) into (12) and simplifying with only known

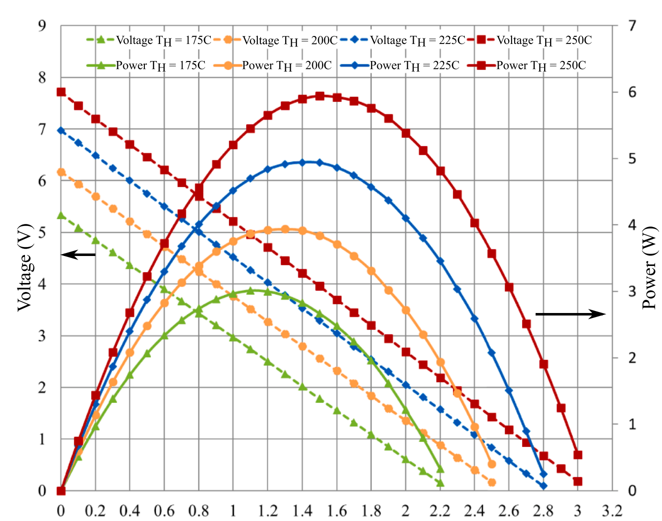

Fig. 4. Experimental electrical characterization of commercial TEG module for T_C = 35 °C.

Table 1
TEG module parameters.

ΔT	V_{oc} [V]	R_{int} [Ohm]	α [V/K]
140	5.33	2.35	0.0381
165	6.17	2.40	0.0374
190	6.97	2.46	0.0367
215	7.72	2.51	0.0359

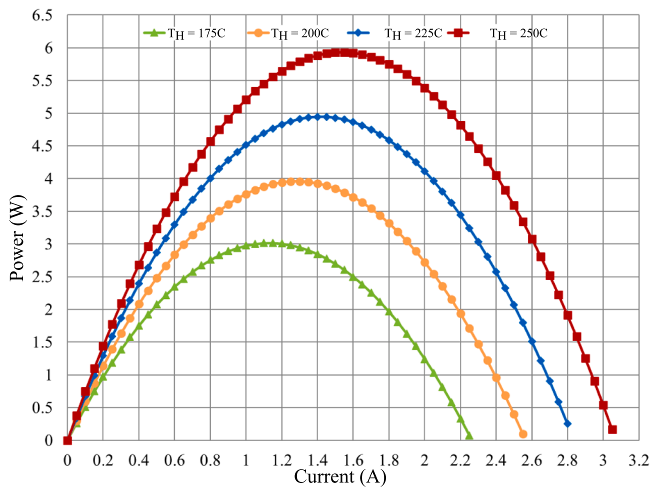

Fig. 5. TEG power output model results for various T_H with $T_C = 35\,°C$.

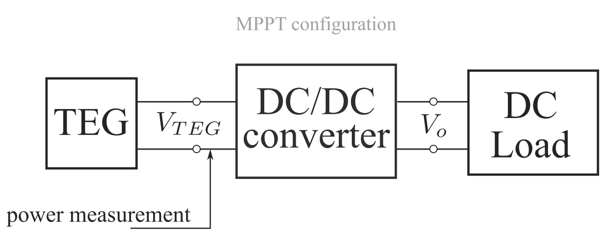

Fig. 6. TEG MPPT configuration.

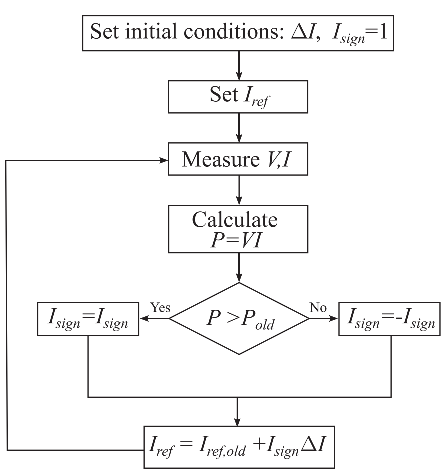

Fig. 7. Perturb & Observe MPPT algorithm.

values (D, V_{oc}, V_o)

$$P = IV_o(1 - D) \tag{14a}$$

$$= \frac{V_{oc}V_o - V_{oc}V_oD - V_o^2 + 2V_o^2D - V_o^2D^2}{R_{int}}. \tag{14b}$$

Assume a sine signal with angular frequency ω and amplitude B is injected into the duty cycle such that $d = D + B\sin(\omega t)$. Substitute d into (14a), the power output of the TEG, and the derivation is the same as (14b) except d is the new duty cycle. The power output, p, due to the duty cycle, d is now

$$\begin{aligned} p =& \; IV_o(1 - d) \\ =& \; \frac{V_{oc}V_o - V_{oc}V_oD - V_o^2 + 2V_o^2D - V_o^2D^2}{R_{int}} + \frac{B\sin(\omega t)(2V_o^2 - 2DV_o^2 - V_{oc}V_o)}{R_{int}} - \frac{B^2\sin^2(\omega t)V_o^2}{R_{int}}. \end{aligned} \tag{15}$$

Rearranging (15), results in

$$p = P + \frac{B\sin(\omega t)[V_o(2V_{TEG} - V_{oc})]}{R_{int}} - \frac{B^2\sin^2(\omega t)V_o^2}{R_{int}}, \tag{16}$$

by identifying that the first term is the power, P, from (14b), and the second term is a function of $(2V_{TEG} - V_{oc})$. It is interesting to note that this term has popped up, since the maximum power of a TEG occurs when the load voltage is equal to the internal voltage, i.e. $V_{TEG} = \frac{1}{2}V_{oc}$, as stated in (8).

Now consider only observing the high frequency terms, which are the second and third term of (16). A high-pass filter is used on p so that only the last two terms of (16) are left, since P is a low frequency term (does not have a sine term). However, since the last term is a $\sin^2$ function, the high-pass filter will extract an offset since this function has an average value. Refer to this offset, or average value as C, which is defined as

$$C = \frac{1}{\omega t}\int_0^{\omega t} \frac{B^2\sin^2(\omega t)V_o^2}{R_{int}} d(\omega t) = \frac{B^2V_o^2}{2R_{int}}. \tag{17}$$

Now (16) is rewritten after a high-pass filter has been applied to p as p_{hp} described by

$$\begin{aligned} p_{hp} =& \; p_1 + p_2 + C \\ p_1 =& \; \frac{B\sin(\omega t)V_o(2V_{TEG} - V_{oc})}{R_{int}} \\ p_2 =& \; -\frac{B^2\sin^2(\omega t)V_o^2}{R_{int}}. \end{aligned} \tag{18}$$

Multiply p_{hp} by $B\sin(\omega t)$ to get p_{sin} to determine whether the term $(2V_{TEG} - V_{oc})$ can be isolated

$$p_{sin} = B\sin(\omega t)p_1 + B\sin(\omega t)p_2 + B\sin(\omega t)C, \tag{19}$$

and apply a low pass filter to p_{sin}, which will again result in an offset, P_{lp} described as

$$P_{lp} = \frac{1}{\omega t}\int_0^{\omega t} p_{sin}\, d(\omega t). \tag{20}$$

By evaluating the average value, (20), P_{lp} is reduced to

$$P_{lp} = \frac{1}{\omega t}\int_0^{\omega t} B\sin(\omega t)p_1\, d(\omega t) = \frac{B^2V_o(2V_{TEG} - V_{oc})}{2R_{int}} \tag{21}$$

since the average value of $\sin^3$ and $\sin$ is always zero over an entire number of periods. The offset, (21), can be negative or zero depending only on the sign of $(2V_{TEG} - V_{oc})$ since the constants $\frac{B^2V_o}{R_{int}}$ are always positive.

By observing the offset from the power after the low pass filter, P_{lp}(21), three different cases arise. *Case 1*: $V_{TEG} = V_{oc}/2$, which makes P_{lp} zero and indicates that the MPP is reached. *Case 2*: $V_{TEG} > V_{oc}/2$ which signifies that the load voltage is higher than $V_{oc}/2$ and results in a positive offset. *Case 3*: $V_{TEG} < V_{oc}/2$ due to the load voltage being lower than $V_{oc}/2$ and equates to a negative offset. The offset, can now be controlled to zero using a PI controller and hence P_{lp} is used as feedback for a proportional integral controller to correct the duty cycle D of the power converter.

The injection frequency is chosen such that it can be resolved well in presence of the power electronic sampling times, e.g. one order of magnitude slower. The high and low pass filter are designed to operate on signals at injection frequency. Hence their bandwidth is chosen at

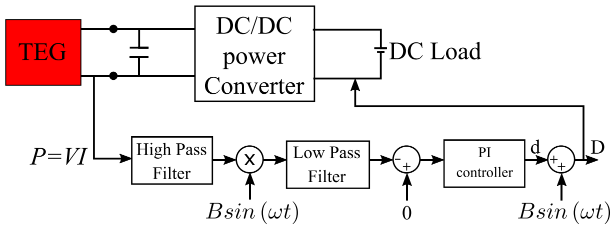

Fig. 8. High Frequency Injection (HFI) MPPT scheme.

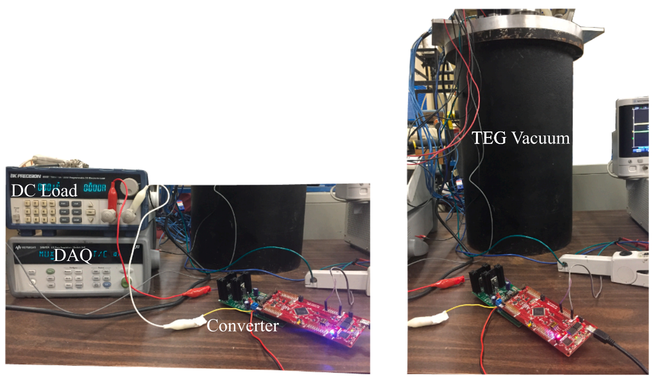

Fig. 9. MPPT experimental setup.

Table 2
Converter efficiency.

I_{in} (A)	V_{in} (V)	P_{in} (W)	P_{out} (W)	η (%)
0.50	9.01	4.51	3.70	82.2
1.10	9.01	9.91	8.29	83.7
1.90	9.01	17.12	14.92	87.2
0.50	12.0	6.0	4.86	80.9
0.95	12.0	11.4	10.15	89.0
1.35	12.0	16.2	14.87	91.7

least one order of magnitude lower than the injection frequency. When the HFI scheme is implemented, the power electronic sampling frequency is chosen as $f_{sw} = 200$ kHz, the injection frequency is 1 kHz, the bandwidth of the high pass filter is 100 Hz, and the bandwidth of the low pass filter is 10 Hz. The injection amplitude, B, is 0.05 V which is 1.25% of the operating TEG voltage. The losses in the converter are estimated to be negligible due to the low magnitude and frequency of the injection signal.

4. MPPT experimental setup

The converter utilized for the experiments was an off-the-shelf evaluation kit from Texas Instruments and the microcontroller is the C2000 TMS320F28377S. The experimental setup for the MPPT experiments is shown in Fig. 9, which has the same electrical configuration as shown in Fig. 6. The TEG module is in the vacuum testing chamber described in Section 2.2 during the MPPT tests performed. For the Perturb & Observe scheme, the closed loop parameters for the current control were $k_p = 0.02$ and $k_i = 7.3 \times 10^{-5}$. For the HFI scheme, the parameters to control the offset, P_{lp} from the low pass filter, to zero were $k_p = 0.05$ and $k_i = 0.01$.

The converter efficiency was also evaluated for various input current and voltages, with the results shown in Table 2.

5. Experimental results

The following sections present the results from the experiments which were completed to evaluate the performance of the proposed HFI MPPT scheme as well as the most-commonly used P&O MPPT scheme. The MPPT experiments were performed with the TEG module that was characterized in Section 2.3. The experimental setup was previously discussed and is shown in Fig. 9.

The experiments were performed to not only compare the HFI scheme to the P&O scheme, but also to compare the HFI results to other experimental work found in the literature. The three experiments conducted were similar to those found in [30], which include thermal transients. The first experiment is a steady-state test which is commonly used to evaluate how well the MPPT scheme finds the MPP. The second experiment is designed to test the response time of the algorithm. The TEG module is at open-circuit and has a fixed temperature difference and suddenly, the tracking scheme is turned-on. This is done to observe how fast the MPPT scheme can find the MPP or half the open circuit voltage. The third experiment is to evaluate how the MPPT scheme performs when the TEG experiences temperature changes (ΔT is not constant). This is a more realistic test, as the TEG will experience temperature fluctuations when implemented in any waste heat recovery applications as previously discussed in Section 1.

5.1. Steady-state performance

The purpose of this steady-state test is to evaluate whether the proposed MPPT scheme- HFI, can accurately track the MPP of the TEG at fixed temperature differences. The MPPs of the TEG module were previously characterized in Section 2.3 for various temperature differences. The P&O scheme was also implemented and tested to have a performance comparison. The steady-state tests were performed as follows: (1) Use the TEG testing facility to reach the desired temperature difference across the TEG, (2) Turn-on the desired tracking scheme (HFI or P&O) and wait for the MPP to be reached while maintaining a fixed temperature difference across the TEG, (3) Wait to reach electro-thermal steady-state and measure the voltage across the TEG module as well as the current flowing through the TEG.

The results of the steady-state tracking performance for both HFI and P&O are shown in Table 3. The first column tabulates the characterization results. The second column presents the operating TEG

Table 3
Steady-state results: (1) Characterization results for various temperature differences, (2) Experimental MPPT Results for both schemes: V_{MP}, Voltage at max power (MP), P_{MP} power output at MP (3) MPPT performance error compared to characterization.

			MPPT Results				MPPT Performance			
	Characterization Results		HFI		P&O		HFI		P&O	
ΔT [C]	V_{MP} [V]	P_{MP} [W]	V_{MP} [V]	P_{MP} [W]	V_{MP} [V]	P_{MP} [W]	V_{MP} [%]	P_{MP} [%]	V_{MP} error [%]	P_{MP} error [%]
140	2.67	3.02	2.57	3.01	2.92–3.24	2.68–2.74	3.56	0.27	9.57–21.58	9.12–11.11
165	3.09	3.95	2.97	3.94	3.35–3.68	3.49–3.54	3.73	0.26	8.59–19.29	10.38–11.65
190	3.49	4.94	3.38	4.93	3.89–4.19	4.43–4.48	3.01	0.17	11.62–20.23	9.37–10.38
215	3.86	5.93	3.76	5.92	4.14–4.86	5.33–5.38	2.59	0.15	7.25–25.91	9.24–10.09

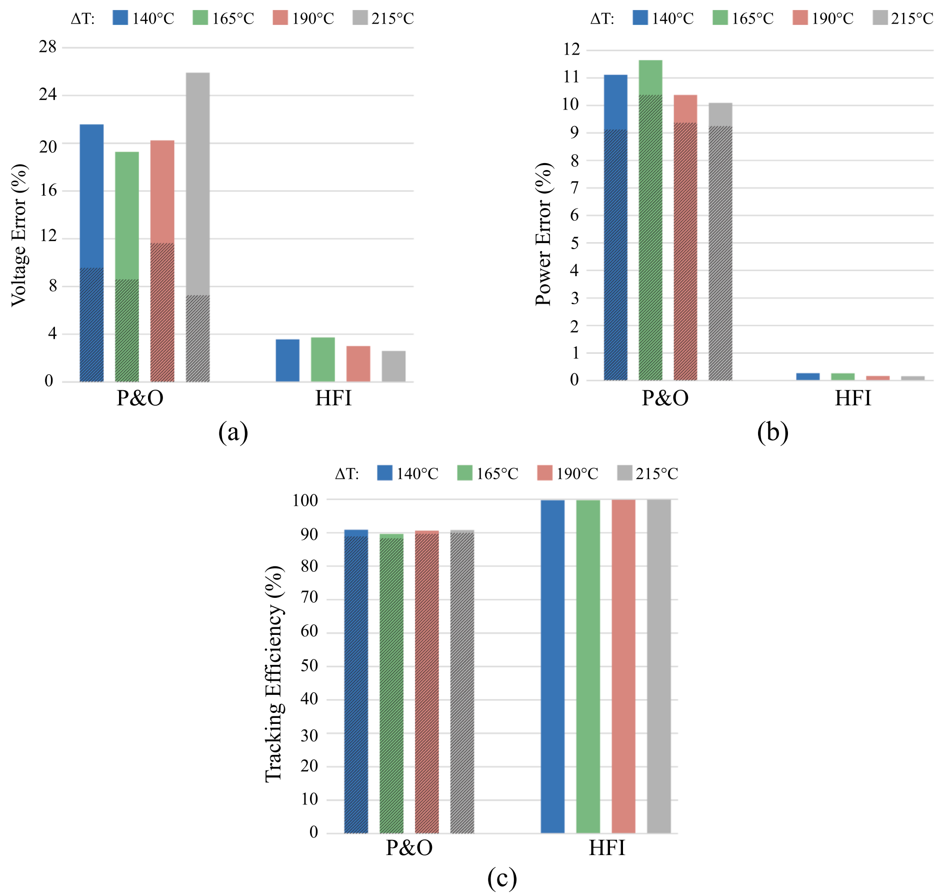

Fig. 10. Steady-State performance from Table 3 represented in graphical form. (a) Voltage error (%) (b) Power error (%) for various temperature differences (ΔT) (c) Comparison of tracking efficiency for the P&O scheme and HFI scheme.

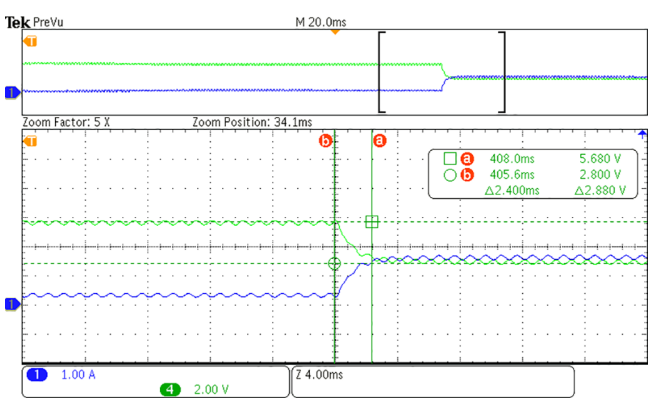

Fig. 11. Transient Evaluation: TEG output voltage changes from V_{oc} to $V_{oc}/2$ when HFI MPPT scheme is turned on. Response time is 2.4 ms.

voltage and power produced by the TEG module for both schemes. Since the P&O scheme oscillates around the MPP, the operating range is presented. The final column shows the error compared to the expected operating TEG voltage and TEG power output (from characterization). The MPPT scheme errors from Table 3 are also presented in graphical form in Fig. 10.

At steady-state the HFI scheme has a tracking efficiency, defined as operating point of the MPPT scheme (P_{op}) divided by the available max power (MP)

$$\eta_{tracking} = \frac{P_{op}}{MP} \tag{22}$$

of 99.73%. However, the tracking efficiency of the P&O scheme is approximately 90% which has previously been found by other researchers [31]. Although more adaptive P&O schemes can be implemented to achieve higher tracking efficiencies such as variable step sizes when approaching the MPP, the purpose of these experiments was to validate the hypothesis that the proposed HFI scheme can accurately track the MPP. The HFI tracking efficiency for various temperature differences is compared to the P&O tracking efficiency in Fig. 10(c). Further work could be done in designing the DC/DC converter to further reduce losses, however this is out of the scope of this paper.

5.2. Fast transient performance

A fast transient test was performed by maintaining the TEG module at a fixed temperature difference and observing the response when the MPPT scheme was turned on. When the HFI scheme is turned on, as seen in the oscilloscope capture of Fig. 11, the TEG voltage changes from 5.68 V and reaches half the open circuit voltage (MPP) of 2.8 V in 2.4 ms. Compared to similar performance evaluations, [30] completed a similar experiment and their MPPT response time was 8 ms, while the researchers [18] had a response of 300 ms. To the best of the authors' knowledge, 2.4 ms is the fastest settling time that has been reported in the literature. The P&O scheme results are not shown since the sampling time of the scheme is 10 ms, as previously mentioned. The electrodynamics need to reach steady-state before the power is measured for the P&O scheme, hence the settling time would be much higher than the HFI scheme.

5.3. Thermal transient performance

The final test to evaluate the performance of the HFI scheme was

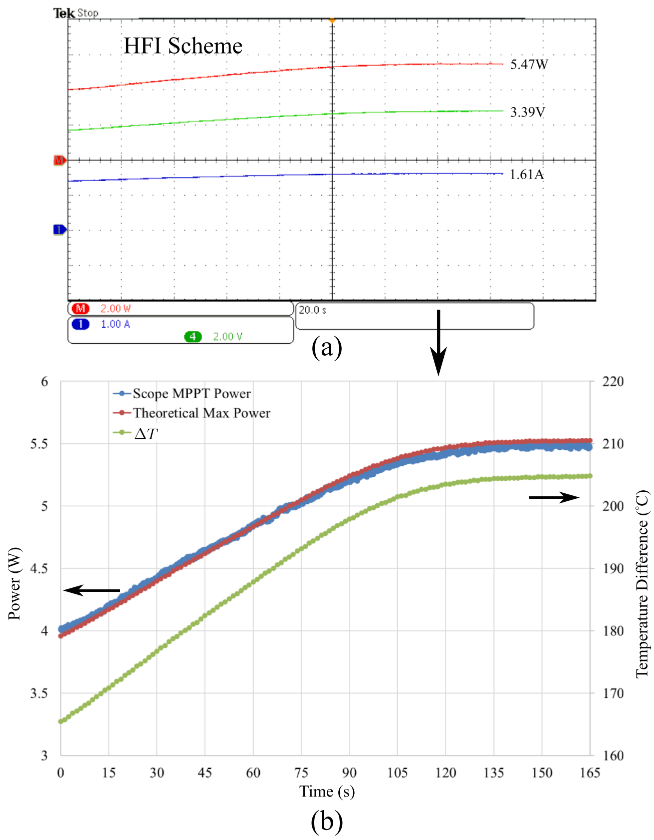

Fig. 12. Thermal transient: (a) Scope screenshot of TEG voltage and current measurement during HFI tracking (b) Comparison of expected power output as a function of temperature difference (ΔT) of the TEG module versus HFI MPPT power.

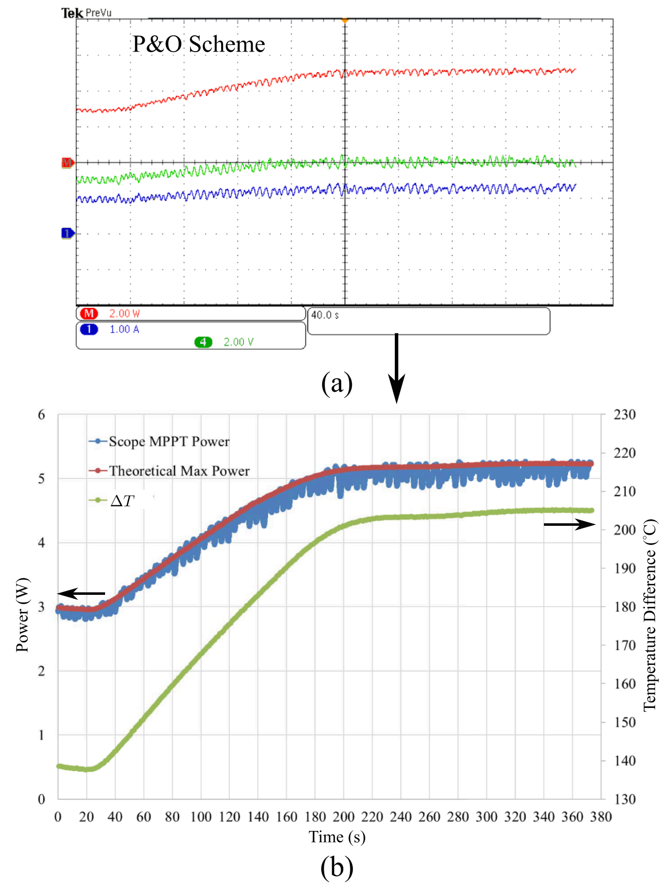

Fig. 13. Thermal transient: (a) Scope screenshot of TEG voltage and current measurement during P&O tracking (b) Comparison of expected power output as a function of temperature difference (ΔT) of the TEG module versus P&O MPPT power.

observing the MPP tracking while the TEG operated under thermal transients. When TEGs harvest energy from waste heat sources such as the exhaust system of a vehicle, they experience variable temperature differences, therefore the MPPT scheme was tested in a transient setting. The test was performed as follows: (1) the TEG module is initially at one temperature difference, (2) the heater power is increased, simultaneously turning on the MPPT scheme, (3) the temperature difference across the TEG is recorded as a function of time, (4) the test is stopped once the temperature stops varying. The temperature difference across the TEG is plotted in green in Fig. 12(b) as a function of time during the tracking of the HFI scheme. The power produced by the HFI scheme is plotted in blue in Fig. 12(b), as well as the theoretical maximum power of the TEG module (red). The theoretical maximum power output of the TEG is calculated from (9) with the parameters from Table 1, since the temperature difference is known every second. The voltage, current, and power generated by the HFI scheme are also shown in the oscilloscope screenshot in Fig. 12(a).

As observed in Fig. 12, the HFI scheme performs well at tracking the MPP over time. The maximum error over the entire time length is 1.3% which makes the tracking efficiency during transient operation 98.7%. The authors in [30] reported the same tracking efficiency during their thermal transient test. Although [32] completed a transient test, their tracking efficiency was not reported and a 0.05 W power output difference was presented over 60 min of tracking.

The P&O scheme was also evaluated during a thermal transient and the results are shown in Fig. 13. As previously discussed, the P&O scheme does not find an exact operating point but instead oscillates around the MPP. Hence, oscillations in the power are observed in Fig. 13(b). The maximum error between the power produced by the P&O MPPT scheme and the expected maximum power is 10%.

6. Conclusion

Thermoelectric generators may be implemented for energy harvesting in waste heat recovery applications. However, to improve the efficiency of the system they need to be interfaced with power converters to ensure the maximum power is generated by the TEG. Since waste heat sources such as the exhaust system of a vehicle vary rapidly in their operating conditions, a maximum power point scheme must be employed to track the varying power output by the TEG system.

In this paper, a High Frequency Injection (HFI) maximum power point tracking scheme was proposed and experimentally validated through three different experiments, as well as compared to the most commonly used MPPT scheme in the literature, P&O. The High Frequency Injection scheme works by adding a high frequency signal to the operation of the TEG, which results in an offset that can be controlled to directly arrive at the TEG's MPP. The experimental results showed that the response time of the proposed MPPT scheme is 2.4 ms which is 3 times faster than any scheme presented in the literature. An advantage of the proposed scheme is that the algorithm can be implemented into current MPPT hardware, i.e. no additional sensors. The HFI scheme was implemented with an off-the-shelf converter and achieved a tracking efficiency at steady state of 99.73%, comparable to the best steady-state tracking schemes while achieving the fastest recorded dynamics. During thermal transients the HFI MPPT exhibited an efficiency of 98.7%.

Declaration of Competing Interest

None.

Acknowledgments

This research was undertaken, in part, thanks to funding from the Canada Excellence Research Chairs (CERC) Program and the Natural Sciences and Engineering Research Council of Canada (NSERC).

References

[1] Aranguren P, Araiz M, Astrain D, Martínez A. Thermoelectric generators for waste heat harvesting: a computational and experimental approach. Energy Convers Manage 2017;148:680–91. https://doi.org/10.1016/j.enconman.2017.06.040.
[2] Watkins C, Shen B, Venkatasubramanian R. Low-grade-heat energy harvesting using superlattice thermoelectrics for applications in implantable medical devices and sensors. ICT 2005. 24th International Conference on Thermoelectrics; vol. 2005. Clemson, SC; 2005 2005. p. 265–7. https://doi.org/10.1109/ICT.2005.1519934.
[3] Thielen M, Sigrist L, Magno M, Hierold C, Benini L. Human body heat for powering wearable devices: from thermal energy to application. Energy Convers Manage 2017;131:44–54. https://doi.org/10.1016/j.enconman.2016.11.005.
[4] Deng F, Qiu H, Chen J, Wang L, Wang B. Wearable thermoelectric power generators combined with flexible supercapacitor for low-power human diagnosis devices. IEEE Trans Ind Electron 2017;64(2):1477–85. https://doi.org/10.1109/TIE.2016.2613063.
[5] Karri M, Thacher E, Helenbrook B. Exhaust energy conversion by thermoelectric generator: two case studies. Energy Convers Manage 2011;52(3):1596–611. https://doi.org/10.1016/j.enconman.2010.10.013.
[6] Liu X, Deng YD, Li Z, Su CQ. Performance analysis of a waste heat recovery thermoelectric generation system for automotive application. Energy Convers Manage 2015;90:121–7. https://doi.org/10.1016/j.enconman.2014.11.015.
[7] LaGrandeur J, Crane D, Hung S, Mazar B, Eder A. Automotive waste heat conversion to electric power using skutterudite, tags, pbte and bite. 2006 25th International Conference on Thermoelectrics, Vienna, Austria 2006. p. 343–8. https://doi.org/10.1109/ICT.2006.331220.
[8] Kempf N, Zhang Y. Design and optimization of automotive thermoelectric generators for maximum fuel efficiency improvement. Energy Convers Manage 2016;121:224–31. https://doi.org/10.1016/j.enconman.2016.05.035.
[9] Lan S, Yang Z, Chen R, Stobart R. A dynamic model for thermoelectric generator applied to vehicle waste heat recovery. Appl Energy 2018;210:327–38. https://doi.org/10.1016/j.apenergy.2017.11.004.
[10] Champier D. Thermoelectric generators: a review of applications. Energy Convers Manage 2017;140:167–81. https://doi.org/10.1016/j.enconman.2017.02.070.
[11] Saidur R, Rezaei M, Muzammil WK, Hassan MH, Paria S, Hasanuzzaman M. Technologies to recover exhaust heat from internal combustion engines. Renewable Sustainable Energy Rev 2012;16:5649–59. https://doi.org/10.1016/j.rser.2012.05.018.
[12] Nagayoshi H, Tokumisu K, Kajikawa T. Evaluation of multi MPPT thermoelectric generator system. 2007 26th International Conference on Thermoelectrics. Jeju Island, South Korea 2007. p. 318–21. https://doi.org/10.1109/ICT.2007.4569487.
[13] Yu C, Chau K. Thermoelectric automotive waste heat energy recovery using maximum power point tracking. Energy Convers Manage 2009;50(6):1506–12. https://doi.org/10.1016/j.enconman.2009.02.015.
[14] Mamur H, Ahiska R. Application of a DC-DC boost converter with maximum power point tracking for low power thermoelectric generators. Energy Convers Manage 2015;97:265–72. https://doi.org/10.1016/j.enconman.2015.03.068.
[15] Park J, Kim S. Maximum power point tracking controller for thermoelectric generators with peak gain control of boost DC-DC converters. J Electron Mater 2012;41(6):1242–6. https://doi.org/10.1007/s11664-011-1884-6.
[16] Liu F, Duan S, Liu F, Liu B, Kang Y. A variable step size INC MPPT method for PV systems. IEEE Trans Ind Electron 2008;55(7):2622–8. https://doi.org/10.1109/TIE.2008.920550.
[17] Kim RY, Lai JS. Optimal design of adaptive maximum-power-point tracking algorithm for thermoelectric based battery energy storage system. 2008 34th Annual Conference of IEEE Industrial Electronics. Orlando, Fl 2008. p. 861–6. https://doi.org/10.1109/IECON.2008.4758066.
[18] Kim RY, Lai JS, York B, Koran A. Analysis and design of maximum power point tracking scheme for thermoelectric battery energy storage system. IEEE Trans Ind Electron 2009;56(9):3709–16. https://doi.org/10.1109/TIE.2009.2025717.
[19] Wu H, Sun K, Chen M, Xing Y. Evaluation of power conditioning architectures for energy production enhancement in thermoelectric generator systems. J Electron Mater 2014;43(6):1567–73. https://doi.org/10.1007/s11664-013-2795-5.
[20] Yamada H, Kimura K, Hanamoto T, Ishiyama T, Sakaguchi T, Takahashi T. A MPPT control method of thermoelectric power generation with single sensor. 2013 IEEE 10th International Conference on Power Electronics and Drive Systems (PEDS). Kitakyushu, Japan 2013. p. 545–58. https://doi.org/10.1109/PEDS.2013.6527152.
[21] Laird I, Lu DDC. High step-up DC/DC topology and MPPT algorithm for use with a thermoelectric generator. IEEE Trans Power Electron 2013;28(7):3147–57. https://doi.org/10.1109/TPEL.2012.2219393.
[22] Park JD, Lee H, Bond M. Uninterrupted thermoelectric energy harvesting using temperature-sensor-based maximum power point tracking system. Energy Convers Manage 2014;86:233–40. https://doi.org/10.1016/j.enconman.2014.05.027.
[23] Paraskevas A, Koutroulis E. A simple maximum power point tracker for thermoelectric generators. Energy Convers Manage 2016;108:355–65. https://doi.org/10.1016/j.enconman.2015.11.027.
[24] Yu S, Du Q, Diao H, Shu G, Jiao K. Effect of vehicle driving conditions on the performance of thermoelectric generator. Energy Convers Manage 2015;96:363–76. https://doi.org/10.1016/j.enconman.2015.03.002.
[25] Ioffe AF. Semiconductor thermoelements and thermoelectric cooling. London: Infosearch Limited; 1957.
[26] Angrist SW. Direct Energy Conversion. 4th ed. Allyn and Bacon, Inc; 1982.
[27] Aashoor FA, Robinson FV. A variable step size perturb and observe algorithm for photovoltaic maximum power point tracking. 2012 47th International Universities Power Engineering Conference (UPEC). London, UK 2012. p. 1–6. https://doi.org/10.1109/UPEC.2012.6398612.
[28] Rodriguez R, Preindl M, Emadi A, Cotton J. Maximum Power Point Tracking for Thermoelectric Generators with High Frequency Injection. 41st Annual Conference of the IEEE Industrial Electronics Society IECON15. Yokohama, Japan 2015. p. 004127–32. https://doi.org/10.1109/IECON.2015.7392744.
[29] Hart Daniel W. Power electronics. McGrawHill9780073380674; 2011.
[30] Montecucco A, Member S, Knox AR, Member S. Maximum power point tracking converter based on the open-circuit voltage method for thermoelectric generators. IEEE Trans Power Electron 2015;30(2):1–12. https://doi.org/10.1109/TPEL.2014.2313294.
[31] Laird I, Lovatt H, Savvides N, Lu D, Agelidis V. Comparative study of maximum power point tracking algorithms for thermoelectric generators. 2008 Australasian Universities Power Engineering Conference. Sydney, Australia 2008. p. 1–6.
[32] Bond M, Park JD. Current-sensorless power estimation and MPPT implementation for thermoelectric generators. IEEE Trans Ind Electron 2015;62(9):5539–48. https://doi.org/10.1109/TIE.2015.2414393.